Slowing-down of non-equilibrium concentration fluctuations in confinement

Cédric Giraudet[1], Henri Bataller[1], Yifei Sun[2], Aleksandar Donev[2], José María Ortiz de Zárate[3] and Fabrizio Croccolo[1]

[1]*Laboratoire des Fluides Complexes et leurs Réservoirs,*
Université de Pau et des Pays de l'Adour, 64600 Anglet, France
[2]*Courant Institute of Mathematical Sciences, New York University, New York, NY 10012, USA and*
[3]*Departamento de Física Aplicada I, Universidad Complutense, 28040 Madrid, Spain*
(Dated: June 12, 2015)

Fluctuations in a fluid are strongly affected by the presence of a macroscopic gradient making them long-ranged and enhancing their amplitude. While small-scale fluctuations exhibit diffusive lifetimes, moderate-scale fluctuations live shorter because of gravity. In this letter we explore fluctuations of even larger size, comparable to the extent of the system in the direction of the gradient, and find experimental evidence of a dramatic slowing-down of their dynamics. We recover diffusive behavior for these strongly confined fluctuations, but with a diffusion coefficient that depends on the solutal Rayleigh number. Results from dynamic shadowgraph experiments are complemented by theoretical calculations and numerical simulations based on fluctuating hydrodynamics, and excellent agreement is found. Hence, the study of the dynamics of non-equilibrium fluctuations allows to probe and measure the competition of physical processes such as diffusion, buoyancy and confinement; i.e. the ingredients included in the Rayleigh number, which is the control parameter of our system.

The physics of systems out of thermodynamic equilibrium is instrumental in several research areas such as physics of fluids, soft matter, astrophysics, statistical physics, biology, metallurgy and many others [1, 2]. As an example, we consider in this letter a binary liquid mixture subjected to a steady temperature gradient parallel to gravity. Two component liquids experience separation in the presence of temperature differences due to different affinities of molecules to 'heat' [3]. A phenomenon referred to as thermodiffusion or Soret effect that will induce a steady concentration gradient in the system. This so-called solutal Rayleigh-Bénard setting, allows for a very refined control of density profiles within the system and the ability to investigate intimate properties of fluids like molecular interactions [4–6].

Any full description of non-equilibrium systems must include spontaneous fluctuations, whose nature is quite different from fluctuations around equilibrium states mainly due to the former long-ranged nature [7–9], not restricted to the proximity of critical points [10]. Non-equilibrium fluctuations are thus a basic problem in understanding transport phenomena like mass diffusion [11], as well as fluctuation-induced, or Casimir, forces [12–14]. In our non-equilibrium problem, the coupling between spontaneous velocity fluctuations and the macroscopic gradient results in giant non-equilibrium concentration fluctuations (c-NEF) in the quiescent state [9, 15]. Gravity quenches the intensity (statics) of fluctuations with length scales larger than a characteristic (horizontal) size $2\pi/q_s^\star$ related to the dimensionless solutal Rayleigh number Ra_s of the system [15, 16]:

$$Ra_s = \frac{\beta_s \vec{g} \cdot \vec{\nabla} c}{\nu D} L^4; \qquad \mid Ra_s \mid = (q_s^\star L)^4, \qquad (1)$$

where $\beta_s = \rho^{-1}(\partial\rho/\partial c)$ is the solutal expansion coefficient, ρ the fluid density, $\vec{g}$ the gravity acceleration, c the concentration (mass fraction) of the denser component of the fluid, $\vec{\nabla} c$ the concentration gradient, D the mass diffusion coefficient, ν the kinematic viscosity, and $q_s^\star$ a characteristic solutal wave vector. This number is the equivalent for the concentration of the Rayleigh number for the temperature and describes the competition of opposite forces like buoyancy, diffusion and boundaries. It is also known that, in addition to gravity, the presence of boundaries further suppress the intensity of c-NEFs with length scales larger than the confinement length L in the direction of the gradient [9, 17].

The role played by the different physical mechanisms (diffusion, buoyancy, confinement) on the *dynamics* of the fluctuations has received comparatively little attention. It is known that gravity accelerates the dynamics of c-NEFs with (horizontal) length scales larger than $2\pi/q_s^\star$ [18, 19]. However, this means that fluctuations of a larger size decay faster, which is a rather non-intuitive behavior [20] and cannot be extrapolated to zero wave number. To investigate these open issues further, we have developed a new shadowgraph machine, with a state-of-the-art CCD detector able to measure at wave vectors down to $q_{\min} = 8.9$ cm^{-1}. Hence, we explored an entire new range of wave numbers, smaller than ever before, and discovered a dramatic slowing-down in the dynamics of c-NEFs. We interpret this slowing-down as caused by confinement, whose role on the dynamics of c-NEFs has not been investigated so far. Our work demonstrates that the study of the dynamics, rather than the intensity, of non-equilibrium fluctuations gives deep insights into the competition of physical processes such as diffusion, buoyancy, and confinement.

Typically, the dynamics of fluctuations is characterized in terms of an Intermediate Scattering Function (ISF

or, equivalently, a normalized time correlation function) $f(q, t)$, with $f(q, 0) = 1$. This function describes how an spontaneous fluctuation of a thermodynamic variable decays in time. In first approximation, the ISF can be modeled by a single exponential, with decay time $\tau(q)$ depending on the fluctuations' wave number q, or length scale in the horizontal directions (perpendicular to gravity and gradient). Available theories accounting for the simultaneous presence of diffusion (d) and gravity (g) [18, 19], but not for confinement, predict for a stable configuration ($Ra_s < 0$):

$$\left.\frac{\tau(\tilde{q})}{\tau_s}\right|_{d+g} = \tilde{\tau}(\tilde{q})|_{d+g} = \frac{1}{\tilde{q}^2 \left(1 - \dfrac{Ra_s}{\tilde{q}^4}\right)}, \quad (2)$$

where the wave vector is expressed in dimensionless form $\tilde{q} = qL$, and $\tau_s = L^2/D$ is the typical solutal time it takes diffusion to traverse the thickness of the sample. Equation (2) implies different behaviors for the decay times of small-scale and large-scale fluctuations, namely, $\tilde{\tau}(\tilde{q})|_d = 1/\tilde{q}^2$ for $\tilde{q} \gg \tilde{q}_s^\star$, and $\tilde{\tau}(\tilde{q})|_g = -\tilde{q}^2/Ra_s$ for $\tilde{q} \ll \tilde{q}_s^\star$. Hence, small length-scale fluctuations decay diffusively and evolve slower the larger the scale. Buoyancy effects, for wave numbers smaller than $q_s^\star$, lead to a non-diffusive decay of fluctuations [20]. Separating these two regimes, the decay time of c-NEFs exhibits a maximum at $\tilde{q}_s^\star$, as clearly shown by Eq. (2). The existence of this maximum, which identifies the most persistent fluctuation in the system if confinement is neglected, has been experimentally demonstrated in a number of experiments on c-NEFs both with a pure concentration gradient (isothermal mass diffusion) [20, 21] or with a concentration gradient induced by the Soret effect [11, 22, 23]. Our purpose here is to go beyond these previous investigations, into a q-range where confinement effects are to be expected.

To observe c-NEFs we used the thermal-gradient cell sketched in Fig. 1: Two sapphire windows kept at fixed vertical distance contain the fluid sample while being thermally controlled by two Peltier elements with a central hole. The entire system allows a quasi-monochromatic parallel light beam pass through in the direction of the temperature gradient. Further details of the thermal gradient cell can be found elsewhere [11, 24]. A stabilizing temperature difference of $\Delta T = 20$ K (with an average temperature of $T_0 = 298$ K) is applied to a horizontal layer of tetralin and n-dodecane at 50% weight fraction. The sample thickness can be varied by using different plastic spacers and sealing O-rings, and for this work three thicknesses $L = 0.7$, 1.3 and 5.0 mm (and a constant lateral extent of $R = 13.0$ mm) were used. The solutal Rayleigh numbers are: $Ra_s = -4 \times 10^4$, -2×10^5 and -1×10^7, respectively [25, 26].

To apply a temperature difference by heating the fluid mixture from above results in a linear temperature profile
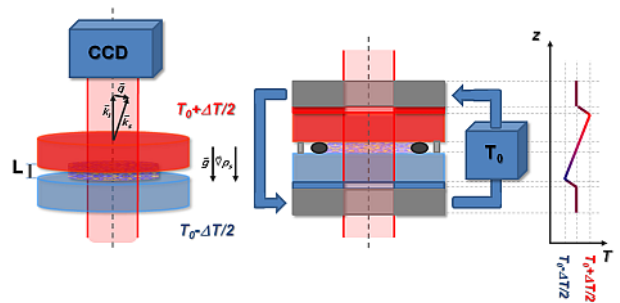

FIG. 1. Experimental cell: two sapphire windows are kept at different temperatures $T_0 + \Delta T/2$ (the top, red one) and $T_0 - \Delta T/2$ (the bottom, blue one) while the sample fluid (colored pattern) is contained by an O-ring (black circles) at a thickness L precisely defined by three plastic spacers (gray rectangles).

across the sample in a thermal time $\tau_T = L^2/\kappa$, where κ is the fluid thermal diffusivity. Due to the smaller value of the mass diffusion coefficient, a nearly linear concentration profile is generated by the Soret effect [1, 27] in a much larger solutal diffusion time $\tau_s = L^2/D$. Since our mixture has a positive separation ratio, for negative Ra_s both the temperature and the concentration profile result in a stabilizing density profile [28].

Shadowgraphy [29–32] allows recording images whose intensities $I(\mathbf{x}, t)$ contain a mapping of the sample refractive-index fluctuations, over space and time, averaged along the direction of the gradient. An example of one of these images is shown in Fig. 2(a). These intensity patterns are generated at the sensor plane by the heterodyne superposition of the light scattered by the sample refractive-index fluctuations and the much more intense transmitted beam ('local oscillator'). Quantitative image analysis is performed by the Differential Dynamic Algorithm [11, 20, 21, 33]. One first computes differences of normalized images $\Delta i_m(\mathbf{x}, \Delta t)$ as shown in Fig. 2(b). These difference images are then 2D-space-Fourier transformed *in silico*, Fig. 2(c), to separate the contribution of light scattered at different wave vectors. This procedure provides results similar to conventional light scattering, but with a shadowgraph one can access much smaller wave vectors. Quantitative image analysis yields the so-called structure function:

$$C(q, \Delta t) = \langle | \Delta i_m(\mathbf{q}, \Delta t) |^2 \rangle_{t, |\mathbf{q}|=q} =$$
$$= \langle | i(\mathbf{q}, t) - i(\mathbf{q}, t + \Delta t) |^2 \rangle_{t, |\mathbf{q}|=q}, \quad (3)$$

with $i(\mathbf{q}, t) = \mathcal{F}[I(\mathbf{x}, t)/\langle I(\mathbf{x}, t)\rangle_{\mathbf{x}}]$ the 2D-Fourier transform of a normalized image $I(\mathbf{x}, t)$ and Δt the time delay between the pair of analyzed images. Examples of experimental $C(q, \Delta t)$ are shown in Fig. 2(d-e).

The physical optics theory of shadowgraphy relates the structure function to the ISF as [11, 20, 21, 33]:

$$C(q, \Delta t) = 2A\{T(q)S(q) \, | \, 1 - f(q, \Delta t) \, | + B(q)\}, \quad (4)$$

where $T(q)$ is the optical transfer function of the instrument (a oscillating function for a shadowgraph, see [30, 31]), $S(q)$ the static structure factor of c-NEFs, A an intensity pre-factor, and $B(q)$ a background including all the phenomena with time-correlation functions decaying faster than the CCD frame rate, such as contributions due to shot noise and temperature fluctuations. Hence, experimental ISF $f(q,t)$ can be evaluated via Eqs. (3)-(4). Results for three different wave vectors are shown in Fig. 2(f).

Essentially, for all the wave vectors accessible in the experiments the ISF can be modeled by a single exponential function. For direct comparison with theory and simulations we extract effective experimental decay times as the time needed to $f(q,t)$ to decay to $1/e$. Figure 3 presents these experimental decay times for the three Ra_s investigated, the raw data in panel (a), and in dimensionless form in panel (b). Note that in Fig. 3(b) for almost all wave vectors smaller than $\tilde{q}_s^\star = \sqrt[4]{-Ra_s}$, the effective decay time departs from the theoretical description of Eq. (2), shown as a dashed line. As the wave vector decreases the decay time presents a minimum for a dimensionless wave vector $\tilde{q}_b \cong 5$, while for smaller wave vectors the decay time recovers a diffusive behavior $\tilde{\tau} \propto \tilde{q}^{-2}$. These conclusions are clear in Fig. 3 except for the larger $Ra_s = -1 \times 10^7$, with no experimental points available at low enough $\tilde{q}$.

To interpret these experimental findings and understand the physical origin of the discovered slowing-down of large-scale c-NEFs, we use a Fluctuating Hydrodynamics (FHD) model [17] that incorporates gravity and confinement. FHD, based on original ideas by Onsager and Landau, supplements dissipative fluxes with random contributions so as to derive in a consistent way a fluctuating or stochastic version of any thermodynamic or hydrodynamic problem [9]. Previous FHD investigations of our problem [17] focused on the intensity (statics) of the c-NEFs. Here we investigate the dynamics and were able to express the theoretical dynamic structure factor as a series of exponentials:

$$S(q)f(q,t) = \sum_{N=1}^{\infty} A_N(q) \exp\left[-\frac{t}{\tau_N(q)} \right], \quad (5)$$

see [34] for further details. The decay times in Eq. (5) are the inverse of the eigenvalues $\Gamma_N(q) = 1/\tau_N(q)$ discussed in Ref. [17]. The amplitudes A_N are analytically related to Γ_N and q. The static structure factor discussed in [17] is then $S(q) = \sum A_N(q)$. In general, the Γ_N can only be computed numerically, however, in the limit $q \to 0$, a full analytical investigation is possible by means of power expansions in q, and a clear hierarchy of well-separated Γ_N can be identified [17]. In that limit, the first amplitude in Eq. (5) dominates, and $f(q \to 0, t)$ becomes a single-exponential in practice, with decay time due to
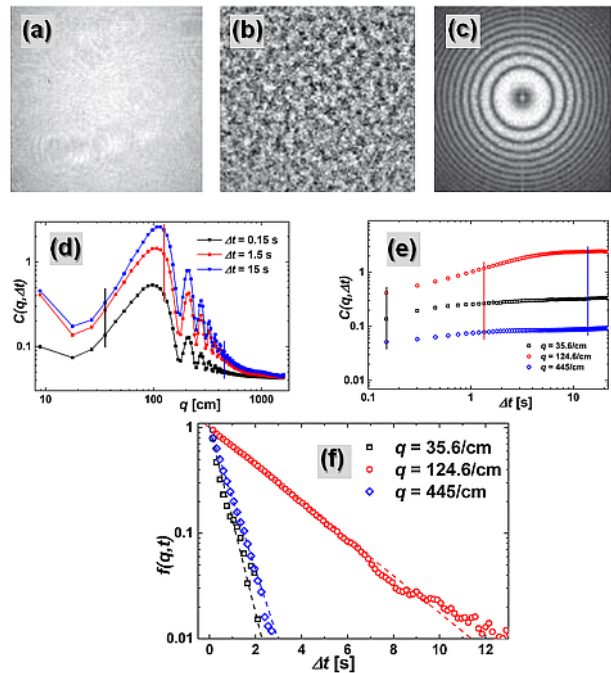

FIG. 2. (a) Shadowgraph image $I(\mathbf{x}, t)$; (b) difference of normalized images $\Delta i_m(\mathbf{x}, \Delta t)$; (c) power spectrum of (b) $| \Delta i_m(\mathbf{q}, \Delta t) |^2$; (d) structure function $C(q, \Delta t)$ for three different time delays, vertical lines stand for wave vectors used in (e); (e) structure function $C(q, \Delta t)$ for three different wave vectors, vertical lines stand for delay times used in (d); (f) ISFs for three different wave vectors $f(q, \Delta t)$: symbols are for experimental data while lines show single-exponential modeling. All data are for $Ra_s = -2 \times 10^5$.

confinement (c):

$$\tilde{\tau}(\tilde{q} \to 0)|_c = \frac{1}{\tilde{q}^2\left(1 - \dfrac{Ra_s}{Ra_{s,c}}\right)} = \frac{1}{\tilde{q}^2\left(1 - \dfrac{Ra_s}{720}\right)}, \quad (6)$$

where $Ra_{s,c} = 720$ is the critical solutal Rayleigh number at which the convective instability appears in this system [28]. Predictions from the asymptotic Eq. (6) are shown in Fig. 3(b) as dotted lines. Hence, the theory shows a crossover from Eq. (2) (not-including confinement) at large and intermediate q, to the confinement behaviour of Eq. (6) at small q, precisely the kind of behaviour experimentally observed. We estimate the wave number q_b corresponding to the minimum decay time by equating Eq. (2) and (6). This gives $\tilde{q}_b = \sqrt[4]{Ra_{s,c}} = \sqrt[4]{720} \cong 5.2$ independent of Ra_s, in further agreement with the experimental observations in Fig. 3(b).

For arbitrary values of q, the decay times $\tau_N(q)$ and corresponding amplitudes can only be evaluated numerically. We have performed a numerical investigation for the experimental Ra_s [34], yielding similar results in the three cases. For very large $\tilde{q} \gtrsim 50$, all decay times collapse to the bulk value, $\tilde{\tau}_N \simeq \tilde{q}^{-2}$, and the ISF is approximately a single exponential. As already commented,

for very small $\tilde{q} \lesssim 0.3$ the first mode dominates in amplitude and a single-exponential decay is again recovered, with decay time given by Eq. (6). For intermediate $0.6 \lesssim \tilde{q} \lesssim 30$, the second mode leads in amplitude but having a smaller decay time means that the two lower modes play a significant role and the theoretical ISF shows signatures of a double exponential decay. Indeed, data from simulations show such signatures in the predicted wave-vector range. However such signatures were not detected in the experiments due to limited range, frame acquisition rate, and insufficient signal to noise ratio. In Fig. 2(e) we reported three examples of experimental ISFs for different wave vectors, with single-exponential modeling.

Regardless of the multiple exponential character, a single effective theoretical decay time $\tau_{\text{eff}}(q)$ can be defined by $f(q, \tau_{\text{eff}}) = 1/e$. In Fig. 3(b) we show results for theoretical $\tau_{\text{eff}}(q)$, computed via Eq. (5) from the numerical decay rates and amplitudes. All the features seen in the experimental data are well reproduced by the theory. Noticeably the slowing-down observed for small wave numbers is clearly related to confinement, since this is the only ingredient added to the 'bulk' theory of Eq. (2).

The FHD theory [17] assumes that viscous dissipation dominates, and neglects the effect of fluid inertia; this is justified by the fact that in all liquids momentum diffusion is much faster than mass diffusion, i.e., the Schmidt number $\text{Sc} = \nu/D$ is very large. While neglecting inertial effects is a good approximation at most wavenumbers of interest, it is known that, depending on Ra_s, it fails at sufficiently small wavenumbers due to the appearance of *propagative modes* [35] (closely related to gravity waves) driven by buoyancy. In order to confirm that the observed slowing down is due to confinement and not to inertia we have performed FHD numerical simulations [36, 37] that account for inertial effects and confinement, see [34] for further details. Data points from a numerical simulation with fluid parameters matching the experimental ones are also displayed in Fig. 3. The excellent agreement of this dataset with experimental and theoretical results, shows that inertia effects are not relevant in our experiments. We note, however, that for thicknesses $L \gtrsim 5$ mm the simulations do show oscillatory time-correlation functions (propagative modes) at the smallest wavenumbers [37], but this range is not accessible in the experiments reported here.

We conclude that, although confinement has a moderate damping impact on the intensities of large-scale non-equilibrium concentration fluctuations [17], in the presence of gravity, it strongly affects their dynamics. Our current findings are in contrast to the case of diffusion in microgravity where the coupling to velocity fluctuations greatly enhances the intensity of the c-NEFs but does not alter their Fickian diffusive dynamics [38].

Although the focus of this letter is on the dynamics and we leave for future publications a full discussion of
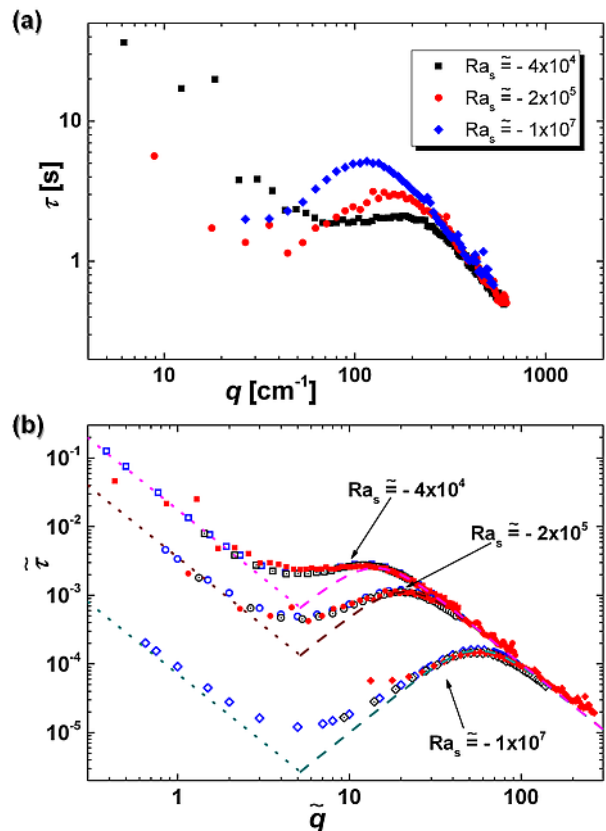

FIG. 3. Effective decay times: (a) Log-log plot of the experimental decay times τ as a function of wave vector q for different Rayleigh numbers. (b) Same in terms of dimensionless variables. In panel (b), filled red symbols are experimental data, open blue are for calculations based on the FHD model, and open-dotted black are from numerical simulations. Dashed curves represent Eq. (2) for $\tilde{q} > \tilde{q}_b$, which accounts for gravity and diffusion only. Dotted lines represent Eq. (6) for $\tilde{q} < \tilde{q}_b$, which accounts for confinement.

the statics, we note that the minimum $\tilde{q}_b$ in τ_{eff} corresponds to a minimum in the intensity of fluctuations $S(q)$. Hence, the current results might be interpreted as a kind of de Gennes narrowing [39]. In analogy to diffusion in colloids, where a competition between interparticle interactions and hydrodynamic effects exists, here we have competition between gravity and confinement.

Interestingly, we find that the dimensionless wave number where confinement coexists with gravity is related to the critical solutal Rayleigh number $Ra_{s,c} = 720$ where the convective instability first appears [28]. This is a signature of the Onsager regression hypothesis stating that the dynamics of the fluctuations contains all of the signatures seen in the deterministic dynamics, which is known to be controlled by the Rayleigh number.

---

[1] S. R. de Groot and P. Mazur, *Nonequilibrium thermodynamics* (North-Holland, Amsterdam, 1962).

[2] S. Kjelstrup and D. Bedeaux, *Non-Equilibrium Thermodynamics Of Heterogeneous Systems* (World Scientific, Singapore, 2008).

[3] S. Hartmann, G. Wittko, W. Köhler, K.I. Morozov, K. Albers, and G. Sadowski, Phys. Rev. Lett. **109,** 065901 (2012).

[4] S. Wiegand, H. Ning, and R. Kita, J. of Non-Equilibrium Thermodynamics **32,** 193 (2007).

[5] G. Galliero, and S. Volz, J. Chem. Phys. **128,** 064505 (2008).

[6] P.-A. Artola, and B. Rousseau, Molecular Physics, **111,** 3394 (2013).

[7] T. R. Kirkpatrick, E. G. D. Cohen, and J. R. Dorfman, Phys. Rev. A **26**, 995 (1982).

[8] J. R. Dorfman, T. R. Kirkpatrick, and J. V. Sengers, Ann. Rev. Phys. Chem. **45**, 213 (1994).

[9] J. M. Ortiz de Zárate and J. V. Sengers, *Hydrodynamic fluctuations in fluids and fluid mixtures* (Elsevier, Amsterdam, 2006).

[10] J. V. Sengers and J. M. H. L. Sengers, Annu. Rev. Phys. Chem. **37,** 189 (1986).

[11] F. Croccolo, H. Bataller, and F. Scheffold, J. Chem. Phys. **137,** 234202 (2012).

[12] T.R. Kirkpatrick, J.M. Ortiz de Zárate and J.V. Sengers, Phys. Rev. Lett. **110,** 235902 (2013).

[13] A. Najafi, and R. Golestanian, Europhys. Lett. **68,** 776 (2004).

[14] A. Hanke, PloS one **8,** e53228 (2013).

[15] A. Vailati and M. Giglio, Nature **390,** 262 (1997).

[16] A. Vailati and M. Giglio, Phys. Rev. E **58,** 4361 (1998).

[17] J. M. Ortiz de Zárate, J. A. Fornés and J. V. Sengers , Phys. Rev. E **74,** 046305 (2006).

[18] P. N. Segrè, R. Schmitz and J. V. Sengers , Physica A **195,** 31 (1993).

[19] P. N. Segrè, and J. V. Sengers , Physica A **198,** 46 (1993).

[20] F. Croccolo, D. Brogioli, A. Vailati, M. Giglio and D. S. Cannell, Phys. Rev. E **76,** 041112 (2007).

[21] F. Croccolo, D. Brogioli, A. Vailati, M. Giglio and D. S. Cannell, App. Opt. **45,** 2166 (2006).

[22] C. Giraudet, H. Bataller, and F. Croccolo, Eur. Phys. J. E, **37,** 107 (2014).

[23] F. Croccolo, H. Bataller, and F. Scheffold, Eur. Phys. J. E, **37,** 105 (2014).

[24] F. Croccolo, F. Scheffold and A. Vailati, Phys. Rev. Lett. **111,** 014502 (2013).

[25] $\rho = 0.8407$ g cm^{-3}, $D = 6.21 \times 10^{-6}$ cm^{2}s^{-1}, $\nu = 1.78 \times 10^{-2}$ cm^{2}s^{-1}, $S_T = 9.5 \times 10^{-3}$ K^{-1}, $\beta_T = 9.23 \times 10^{-4}$ K^{-1}, $\beta_s = 0.27$, $\psi = c_o(1 - c_o)S_T\beta_s/\beta_T = 0.695$, $\kappa = 9.7 \times 10^{-4}$ cm^{2}s^{-1} from [26] and references therein.

[26] J. K. Platten, M. M. Bou-Ali, P. Costesèque, J. F. Dutrieux, W. Köhler, C. Leppla, S. Wiegand, and G. Wittko, Phil. Mag. **83,** 1965 (2003).

[27] C. Soret, Arch. Sci. Phys. Nat. **3,** 48 (1879).

[28] A. Ryskin, H. W. Müller, and H. Pleiner, Phys. Rev. E **67,** 046302 (2003).

[29] G. S. Settles, *Schlieren and Shadowgraph Techniques* (Springer, Berlin, 2001).

[30] S. Trainoff, and D. S. Cannell, Phys. Fluids **14,** 1340 (2002).

[31] F. Croccolo, and D. Brogioli, App. Opt. **50,** 3419–3427 (2011).

[32] The probing beam is a plane parallel beam of quasi-monochromatic light as in previous setups [11, 24]. After the sample no collecting lens is used. A Charged Coupled Device sensor (IDS, UI-6280SE-M-GL) with a resolution of 2448×2048 pixels of $3.45 \times 3.45 \mu m^2$ is placed at a distance of $z = (100 \pm 10)$ mm from the detector. Images are cropped to square resolution of 2048×2048 pixels. In this arrangement the size of the image is dictated by the real size of the CCD sensor, which is 7.066 mm. This fixes the minimum wave vector to $q_{\min} = 8.89$cm^{-1}.

[33] R. Cerbino, and V. Trappe, Phys. Rev. Lett. **100,** 188102 (2008).

[34] C. Giraudet, H. Bataller, Y. Sun, A. Donev, J. M. Ortiz de Zárate and F. Croccolo, http://arxiv.org/abs/1410.6524

[35] C. J. Takacs, G. Nikolaenko and D. S. Cannell, Phys. Fluids **100,** 234502 (2008).

[36] F. Balboa Usabiaga, J. B. Bell, R. Delgado-Buscalioni, A. Donev, T. G. Fai, B. E. Griffith, and C. S. Peskin, SIAM J. Multiscale Model. Simul. **10,** 1369 (2012).

[37] S. Delong, Y. Sun, B.E. Griffith, E. Vanden-Eijnden and A. Donev, Phys. Rev. E, **90,,** 063312 (2014).

[38] A. Vailati, R. Cerbino, S. Mazzoni, C. J. Takacs, D. S. Cannell and M. Giglio, Nature Comm. **2,** 290 (2011).

[39] P. G. de Gennes, Physica A **25**, 825 (1959).